Journal of Nanomaterials and Applications

Journal homepage: https://jna.com.vn

Strain-Rate-Dependent Tensile Deformation and Fracture of Monolayer Amorphous Graphene: A Reactive Molecular Dynamics Study

Nguyen Dac Dien [1], **Dung Nguyen Trong** [2,*], **Umut Saraç** [3]

[1] Faculty of Occupational Safety and Health, Vietnam Trade Union University, 169 Tay Son, Kim Lien, 100000, HaNoi, Vietnam.

[2] Faculty of Application Science, University of Transport Technology, 54 Trieu Khuc, Thanh Xuan, 100000, HaNoi, Vietnam.

[3] Department of Science Education, Bartın University, 74100 Bartın, Turkey.

Article info

Type of articles:
Original research paper

Corresponding author*:
Dung Nguyen Trong
dungnt78@utt.edu.vn

Received: 15 August 2026
Revised: 21 September 2026
Accepted: 23 September 2026
Published: 28 September 2026

Abstract: Amorphous graphene (a-graphene) a 2D carbon network with short-range order but no long-range periodicity holds promise for flexible electronics and nanocoatings, yet its rate-dependent mechanics remain unclear. Reactive molecular dynamics (MD) simulations using the ReaxFF potential investigated the tensile deformation and fracture of monolayer a-graphene at 300 K. The stress–strain behavior exhibits linear elasticity, non-linear yielding, and abrupt fracture. At a baseline strain rate of $\dot{\varepsilon} \approx 10^9$ s^{-1}, the effective Young's modulus is 345.2 GPa (~1/3 of pristine graphene) due to topological disorder and non-hexagonal (5-7-8) ring defects. Increasing the strain rate 2.5-fold to $\dot{\varepsilon} \approx 2.5 \times 10^9$ s^{-1} elevates the ultimate tensile strength from 138.2 to 158.0 GPa and fracture strain from 0.0933 to 0.1158. Failure initiates via stress concentration at under-coordinated defects, leading to micro-void nucleation, coalescence, and brittle cleavage. This rate sensitivity stems from competition between loading rate and thermal relaxation of strained C–C bonds.

Keywords: Amorphous graphene; ReaxFF; Molecular dynamics; Strain-rate sensitivity; Tensile fracture; Mechanical properties

1. Introduction

Since its isolation, monolayer graphene has attracted intense interest owing to its exceptional mechanical strength, high electrical conductivity, and large specific surface area, which make it a foundational material

for nanoelectronics, supercapacitors, and structural nanocomposites [1–16]. Pristine crystalline graphene combines an intrinsic Young's modulus of about 1 TPa with a tensile strength of about 130 GPa [8, 17, 18]; however, producing defect-free, large-area sheets remains challenging [19–21]. Real graphene samples therefore inevitably contain point defects, grain boundaries, and disordered regions. In the limit of complete disorder, two-dimensional amorphous graphene (a-graphene) a carbon monolayer with short-range atomic order but no long-range translational symmetry emerges as a distinct class of carbon nanomaterials [22-24]. Topological defects predominantly non-hexagonal rings, such as clusters of five-, seven-, and eight-membered rings perturb the local bonding environment and stress distribution and thereby alter the mechanical performance of a-graphene relative to its crystalline counterpart [24–28]. Previous computational studies have examined the elastic properties of graphene-derived structures [17, 18, 29–33,] and their surface functionalization behavior. Nevertheless, the deformation regimes and the strain-rate sensitivity of single-layer a-graphene remain insufficiently understood, particularly when bond breaking and bond formation are described by a reactive force field. Such knowledge is essential for understanding how rapid, high-rate loading affects failure criteria, atomic-scale cleavage, and energy redistribution, and hence for designing resilient flexible electronics and protective coatings [34–36]. Furthermore, in recent years, members of the research team have successfully investigated the factors influencing the mechanical properties of nickel materials [37] and epoxy thin films [38]. The results indicate that these factors have a significant impact on the mechanical properties. Reactive molecular dynamics (MD) is well suited to this problem because, unlike fixed-topology empirical potentials, the ReaxFF potential allows bonds to form and break dynamically and therefore describes the fracture process naturally. In this work, ReaxFF-based MD simulations are conducted to systematically investigate the uniaxial tensile response of monolayer a-graphene and, in particular, its dependence on the strain rate. The specific objectives are (i) to determine the effective Young's modulus, ultimate tensile strength, and fracture strain and to compare them with those of pristine graphene; (ii) to identify the characteristic deformation states and the atomic-scale mechanisms of void nucleation and crack propagation; and (iii) to clarify how the loading rate governs the strength and extensibility of the amorphous network. The remainder of the paper is organized as follows: Section 2 describes the computational methodology, Section 3 presents and discusses the results, and Section 4 summarizes the main conclusions.

2. Computational methodology

2.1. Simulation model

The monolayer a-graphene sheet consisted of $\mathrm{N} = 1600$ carbon atoms placed in a rectangular simulation cell with dimensions of $\mathrm{L_x} \approx 65.2\text{Å}$ and $\mathrm{L_y} \approx 64.8\text{Å}$ along the in-plane directions. A vacuum spacing of 20Å was imposed along the perpendicular z-axis to eliminate artificial inter-layer interactions between periodic images. The two-dimensional amorphous network was generated using a melt-quench protocol via molecular dynamics simulations, wherein a pristine crystalline graphene lattice was initially melted at $4500\ \mathrm{K}$ and subsequently quenched to $300\ \mathrm{K}$ at a controlled cooling rate of $10\ \mathrm{K/ps}$. The structural

topology of the resulting network was characterized by ring statistics, comprising 12.5% pentagons (5-membered), 68.4% hexagons (6-membered), 14.2% heptagons (7-membered), and 4.9% octagons (8-membered). The short-range disorder and lack of long-range periodicity were further confirmed by the radial distribution function (RDF, $g(r)$).

An effective sheet thickness of 3.4 Å was assumed to convert the atomic-level stresses into volumetric stress values. Periodic boundary conditions were imposed along all three orthogonal directions (x, y, and z).

2.2. Interatomic potential

All simulations were performed with the Large-scale Atomic/Molecular Massively Parallel Simulator (LAMMPS) package. Atomic interactions within the amorphous carbon network were described by the ReaxFF reactive force field [1, 39], using the parameter set developed [40] for carbon condensed phases (specifically ffield.reax.cho / C-2015), in which bond orders are computed dynamically from interatomic distances so that bonds can break and form during deformation. The total potential energy of the system, E_{system}, is expressed as the sum of partial energy contributions:

$$E_{system} = E_{bond} + E_{over} + E_{under} + E_{val} + E_{pen} + E_{tors} + E_{VDW} + E_{Coulomb} \quad (1)$$

where E_{bond}, E_{over}, E_{under}, E_{val}, E_{pen}, E_{tors}, E_{VDW}, and $E_{Coulomb}$ denote the bond energy, the over-coordination penalty, the under-coordination stability term, the valence-angle energy, the penalty energy, the torsion energy, the non-bonded van der Waals energy, and the Coulomb (electrostatic) energy, respectively [39].

2.3. Equilibration and tensile loading

Prior to mechanical loading, the initial configuration was relaxed for 100 ps in the isothermal–isobaric (NPT) ensemble at $T = 300\ K$ and $P = 0\ GPa$ using a Nosé–Hoover thermostat–barostat to eliminate residual stresses. Uniaxial tensile loading was then applied along the x -axis in the NPT ensemble at $T = 300\ K$, where a constant strain rate was imposed along the loading direction while the lateral stress along the y -axis was coupled to a Nosé–Hoover barostat set at $P_y = 0\ GPa$ to maintain a stress-free lateral boundary condition (allowing lateral Poisson contraction).

Table 1. Integration time steps and the corresponding effective strain rates. Values other than the two limiting cases are derived assuming a constant strain increment per step.

Case	h (fs)	Relative strain rate	$\dot{\varepsilon}$ ($10^9\ s^{-1}$)
h_4	2.5	1.00	≈ 1.00
h_3	2.0	1.25	≈ 1.25
h_2	1.5	1.67	≈ 1.67
h_1	1.0	2.50	≈ 2.50

To examine the strain-rate sensitivity while maintaining numerical stability, four integration time steps, h = 2.5, 2.0, 1.5, and 1.0 fs, were used with a constant strain increment $\Delta\varepsilon$ applied at every step, so that the

effective strain rate scales as $\dot{\varepsilon} = \Delta\varepsilon/h$. The baseline condition (h = 2.5 fs) corresponds to $\dot{\varepsilon} \approx 10^9\ s^{-1}$; decreasing h to 1.0 fs therefore increases the effective strain rate by a factor of 2.5, to $\dot{\varepsilon} \approx 2.5 \times 10^9\ s^{-1}$ (Table 1). A constant strain increment of $\Delta\varepsilon = \dot{\varepsilon}h \approx 2.5 \times 10^{-6}$ per step is implied by the two limiting cases.

2.4. Stress and property evaluation

The atomic stress tensor was monitored throughout the simulations using the virial formulation:

$$\sigma_{ij} = (1/V)\ [\ -\Sigma_k\ m_k\ v_i^k\ v_j^k + \tfrac{1}{2}\ \Sigma_k\ \Sigma_{l\neq k}\ r_i^{kl}\ F_j^{kl}\ ] \qquad (2)$$

where V is the effective volume (the sheet area multiplied by the effective thickness), m_k and v^k are the mass and velocity of atom k, r^{kl} is the interatomic distance vector, F^{kl} is the interatomic force vector between atoms k and l, and i and j denote Cartesian components. The axial stress σ_{xx} was plotted against the applied strain ε to obtain the stress–strain curves. The Young's modulus E was determined from the slope of the curve in the initial linear-elastic regime ($\varepsilon < 0.03$) using Hooke's law, $\sigma = E\varepsilon$. The ultimate tensile strength (UTS, σ_{UTS}) was taken as the maximum stress, and the fracture strain ε_f as the strain at which this maximum occurs and after which the stress drops abruptly. For comparison with other two-dimensional materials, the modulus is also expressed as a two-dimensional quantity, $E_{2D} = Et$, with t = 3.4 Å.

3. Results and discussion

3.1. Structural model and stress–strain response

Figure 1 shows the atomic model (panels a and b), the stress–strain response of single-layer a-graphene under uniaxial tension along the x-axis (panels c–e), and the evolution of the total energy with strain (panel g). The Young's modulus was evaluated in the initial linear-elastic regime ($\varepsilon < 0.03$) using Hooke's law ($\sigma = E\varepsilon$). Under the baseline loading condition (h = 2.5 fs), the effective Young's modulus of the a-graphene sheet is $E \approx 345.2$ GPa (Table 2), i.e. about 35% of that of pristine monolayer graphene (~1 TPa). Expressed as a two-dimensional modulus, this corresponds to $E_{2D} \approx 117$ N m^{-1}, compared with ≈ 340–370 N m^{-1} for pristine graphene at the same effective thickness. This reduction is attributed to the topological 5-7-8 ring defects, which distort the local bond angles of the sp^2 network and reduce the effective density of load-bearing C–C bonds along the loading path.

Table 2. Mechanical properties of monolayer a-graphene (this work) compared with values quoted for pristine graphene.

Material system	Potential	E (GPa)	E_{2D} (N m^{-1})	σ_{UTS} (GPa)	Fracture strain ε_f
Pristine graphene	AIREBO / ReaxFF	~1000–1080	~340–370	~120–130	~0.15–0.20
a-Graphene (h = 2.5 fs)	**ReaxFF** (this work)	**345.2**	**117.4**	**138.2**	**0.0933**
a-Graphene (h = 1.0 fs)	**ReaxFF** (this work)	**358.6**	**121.9**	**158.0**	**0.1158**

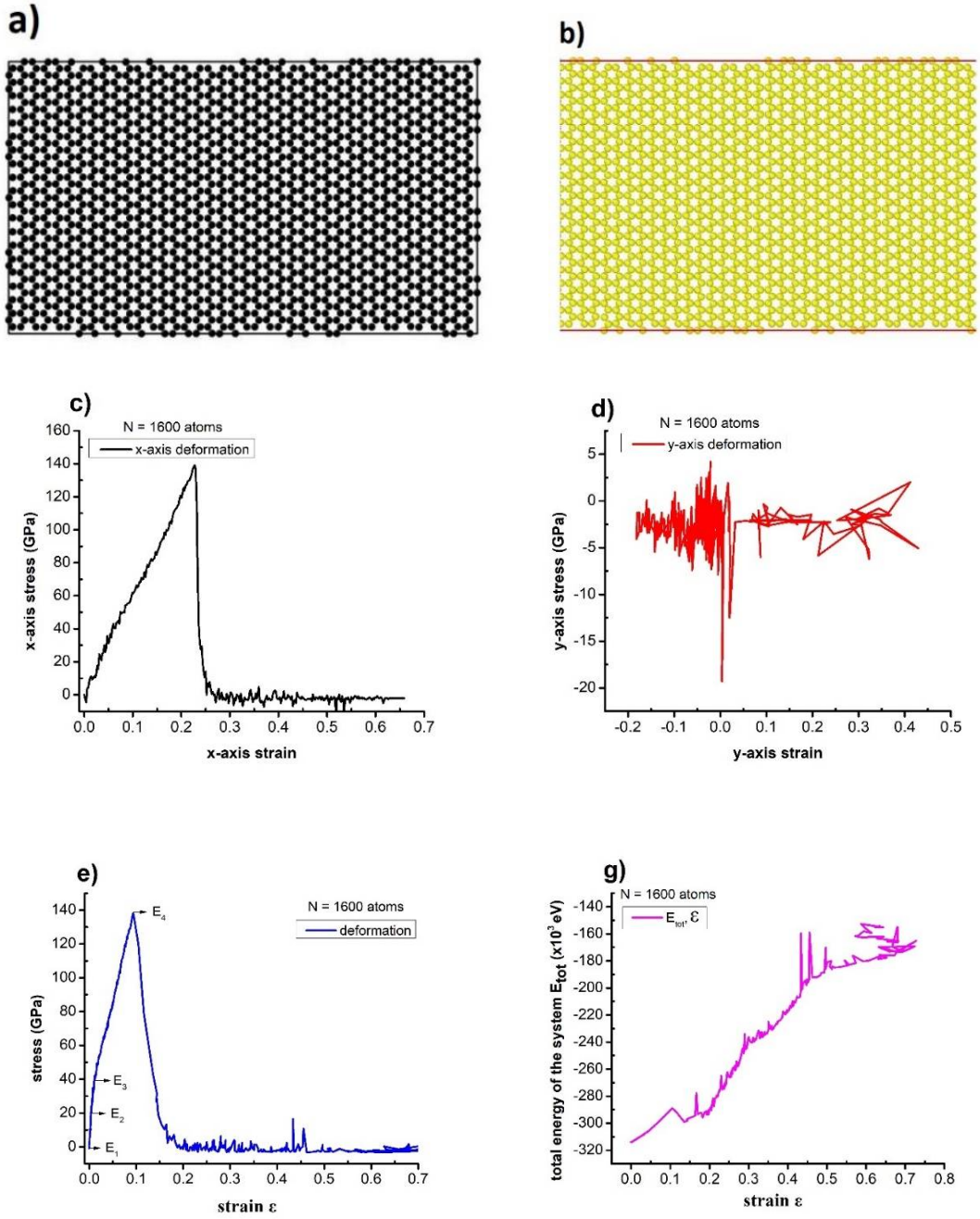

Figure 1. Structural model and mechanical response of monolayer amorphous graphene under uniaxial tension along the x-axis (N = 1600 atoms, T = 300 K, P = 0 GPa, h = 2.5 fs): (a, b) atomic model of the a-graphene sheet; (c) axial stress–strain curve; (d) transverse (y-axis) stress–strain curve; (e) stress–strain curve with the characteristic states marked; and (g) variation of the total energy of the system with strain.

E_{2D} = Et with t = 3.4 Å. Pristine-graphene values are the literature ranges quoted in the Introduction and were obtained under different conditions (potential, strain rate); the comparison is therefore indicative only.

The axial stress increases with strain up to a well-defined maximum and then drops abruptly (Figure 1c,e), whereas the transverse stress remains small in comparison (Figure 1d), consistent with predominantly

uniaxial loading. The total energy of the system increases with strain (Figure 1g) as elastic energy is stored in the stretched C–C bonds, with irregular fluctuations appearing only at large strains, after failure. The a-graphene sheet also fails at a smaller strain (ε_f = 0.0933) than the ~0.15–0.20 quoted for pristine graphene (Table 2), indicating that the defective network is less extensible than the crystalline lattice. Its tensile strength, in contrast, is comparable to or higher than the quoted pristine range, which may partly reflect the much higher strain rate employed here.

3.2. Deformation stages and failure mechanism

The tensile deformation of a-graphene can be described by four characteristic states, marked in Figure 1 and 2 and summarized in Table 3, which delineate three regimes: linear elasticity, non-linear yielding, and fracture.

Table 3. Characteristic states along the stress–strain curve of a-graphene (h = 2.5 fs).

State	Strain	Deformation stage	Dominant atomic-scale event
1	$\varepsilon < 0.03$	Linear elastic regime	Uniform stretching of C–C bonds with negligible structural rearrangement.
2	$\varepsilon \approx 0.05$	Non-linear yielding	Onset of localized stress concentrations near non-hexagonal ring clusters, with minor bond-angle adjustments.
3	$\varepsilon \approx 0.09$	Peak stress (UTS)	Maximum load capacity, σ_{UTS} = 138.2 GPa; micro-voids initiate through the first C–C bond cleavage at highly distorted pentagon–heptagon junctions.
4	$\varepsilon > 0.12$	Crack propagation and fracture	Rapid coalescence of nano-voids leading to brittle-like catastrophic failure across the sheet width, perpendicular to the loading direction.

Atomistic snapshots in Figure 2 confirm these mechanisms. At state 1 (Figure 2a1–a3), which represents the initial unstrained configuration (ε = 0), the carbon atoms retain their isotropic, disordered arrangement. As the strain increases through state 2 (Figure 2b1–b3) and state 3 (Figure 2c1–c3), the C–C bonds elongate significantly along the x-axis, accompanied by Poisson contraction along the y-axis.

The out-of-plane side views (Figure 2b2, c2) indicate slight ripple formation (buckling), which further accommodates the strain energy. At state 4 (Figure 2d1–d3), severe stress concentrations trigger bond rupture and the detachment of atoms from their lattice sites, and the sheet enters the fracture regime, characterized by voids in the plane and strong out-of-plane distortion of the failed sheet. The failure sequence stress concentration at under-coordinated defect nodes, micro-void nucleation at strongly distorted five–seven junctions, void coalescence, and rapid cleavage indicates that the non-hexagonal ring clusters act as the weak links that control the strength of the amorphous network.

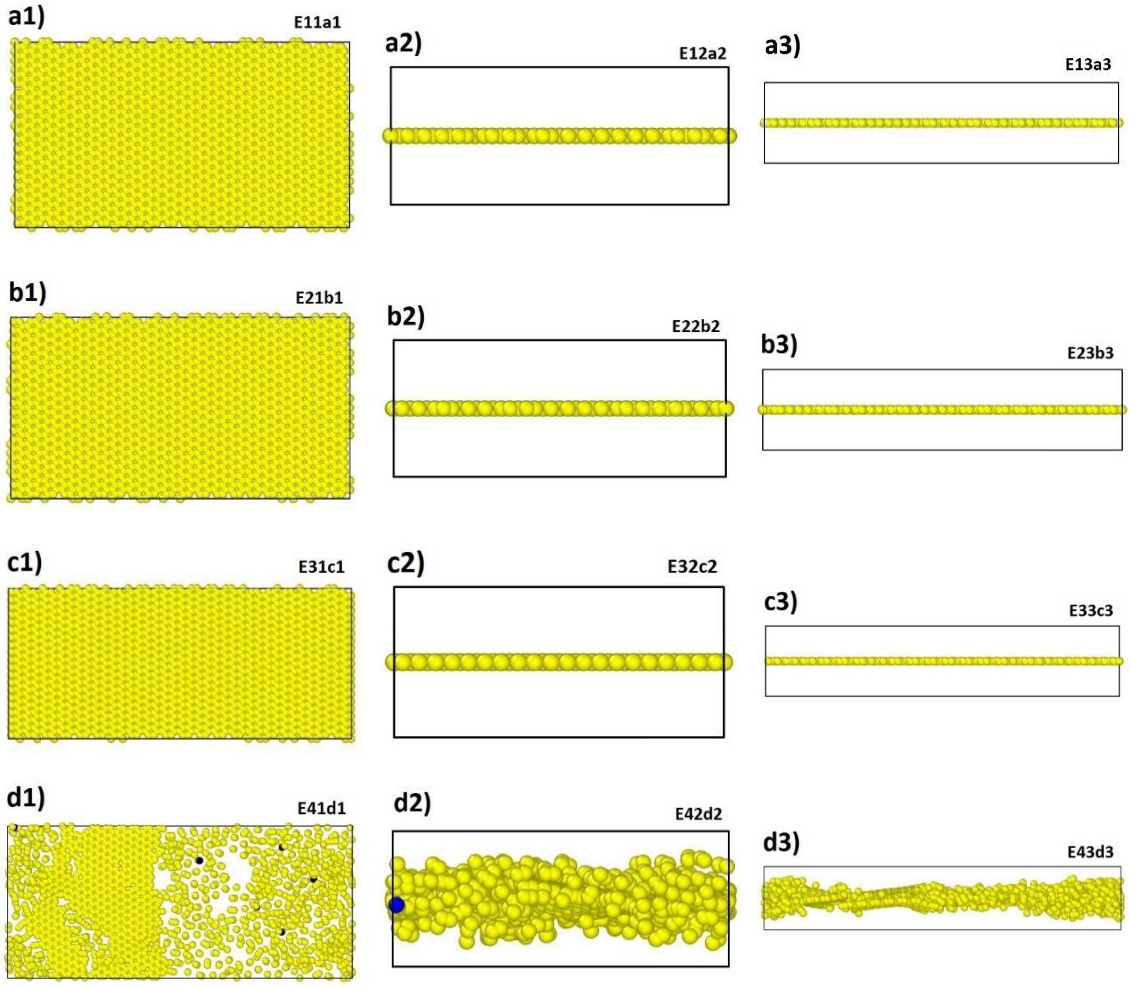

Figure 2. Atomic configurations at the four characteristic states (1–4) during uniaxial tension (columns 1–3: top view and side views): (a) initial state at state 1; (b) deformation evolution at state 2; (c) advanced strain accumulation at state 3; and (d) critical elastic limit followed by void nucleation and atom detachment at state 4.

3.3. Effect of strain rate

Figure 3 compares the stress–strain curves obtained with h = 2.5, 2.0, 1.5, and 1.0 fs, i.e. for effective strain rates from $\approx 1 \times 10^9$ to $\approx 2.5 \times 10^9$ s^{-1} (Table 1). All curves share the same qualitative features a steep initial rise, a sharp maximum, and an abrupt stress drop but both the peak stress and the peak strain increase as h decreases. Reducing h from 2.5 fs to 1.0 fs raises the UTS from 138.2 GPa (ε_f = 0.0933) to 158.0 GPa (ε_f = 0.1158), i.e. by 14.3% and 24.1%, respectively, and slightly increases the Young's modulus from 345.2 to 358.6 GPa (+3.9%; Table 2). The curves for the intermediate time steps lie between the two limiting cases, indicating a systematic strain-rate hardening.

This strain-rate hardening reflects the competition between the imposed deformation rate and the internal relaxation kinetics of the strained C–C bonds. At the lower strain rate (h = 2.5 fs), atoms have sufficient time for thermally assisted structural rearrangement and stress redistribution around the topological defect nodes, so that micro-voids nucleate at lower stress levels. At the higher strain rate (h = 1.0 fs), the loading outpaces the natural relaxation time scale of the amorphous network; the system lacks the time for

kinetic stress relief, and the strained C–C bonds temporarily sustain higher stress before catastrophic bond cleavage occurs. In the framework of thermally activated bond rupture, a higher loading rate reduces the time available for thermal fluctuations to overcome the stress-lowered energy barrier for bond breaking, which shifts the failure stress and strain upward. The absolute values obtained at MD strain rates of the order of 10^9 s^{-1} should nevertheless be regarded as upper bounds for quasi-static loading, because MD strain rates exceed experimental ones by many orders of magnitude.

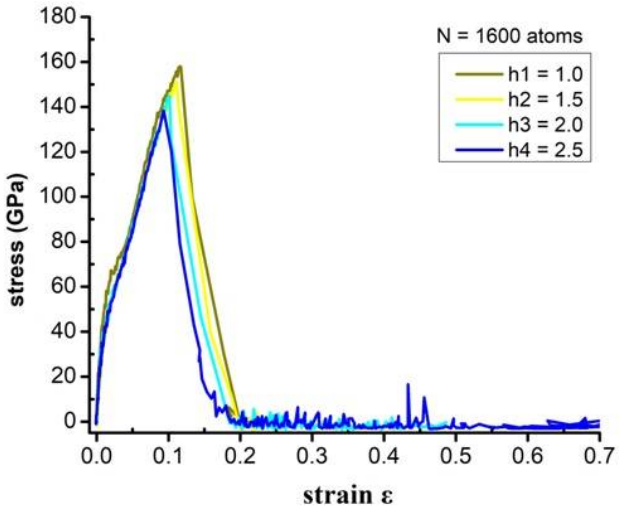

Figure 3. Influence of the strain rate (time steps h = 1.0, 1.5, 2.0, and 2.5 fs) on the mechanical response and stress–strain relationships of single-layer amorphous graphene (N = 1600 atoms).

3.4. Implications and limitations

The results show that the strength of a-graphene is not a fixed material constant but depends on the loading rate, which must be taken into account when design parameters for flexible electronics or protective coatings are extracted from MD simulations. Although the modulus of a-graphene is only about one third of that of the crystalline lattice, the sheet sustains stresses of 138–158 GPa and strains of about 9–12% before failure under the present loading conditions.

Several limitations should be kept in mind. First, the simulations refer to a single 1600-atom configuration at 300 K and to a narrow window of strain rates (≈ 1–2.5 × 10^9 s^{-1}); larger systems, several independent amorphous configurations, and wider ranges of temperature and strain rate would allow the statistical scatter and the functional form of the rate dependence to be quantified. Second, the accuracy of the reactive force field for highly distorted, under-coordinated carbon configurations close to fracture should be benchmarked against first-principles calculations or alternative interatomic potentials. These aspects will be addressed in future work.

4. Conclusions

In summary, reactive molecular dynamics simulations based on the ReaxFF potential were employed to investigate the mechanical behavior and strain-rate sensitivity of single-layer amorphous graphene under uniaxial tension. The main conclusions are as follows: Topological ring defects reduce the effective Young's

modulus of a-graphene to E ≈ 345.2 GPa (about 35% of that of pristine graphene) because of stress concentration at non-hexagonal ring nodes. The tensile process passes through four characteristic states—linear Hookean elasticity, non-linear yielding, peak-stress void initiation, and catastrophic brittle-like cleavage with fracture initiated at under-coordinated defect nodes. Increasing the effective strain rate from $\approx 1 \times 10^9$ to $\approx 2.5 \times 10^9$ s^{-1} (decreasing h from 2.5 to 1.0 fs) enhances the UTS from 138.2 to 158.0 GPa and the fracture strain from 0.0933 to 0.1158, owing to the limited thermal relaxation available within the amorphous lattice at higher loading rates.

Funding: This research received no external funding.

Data availability statement: The data that support the findings of this study are available from the corresponding author upon reasonable request.

Declaration of competing interest: The authors declare that they have no known competing financial interests or personal relationships that could have appeared to influence the work reported in this paper.

References

[1] A.C.T. van Duin, S. Dasgupta, F. Lorant, W.A. Goddard, (2001). ReaxFF: a reactive force field for hydrocarbons. J. Phys. Chem. A, 105(41), 9396–9409. https://doi.org/10.1021/jp004368u

[2] A.C. Ferrari, F. Bonaccorso, V. Fal'ko, K.S. Novoselov, S. Roche, P. Bøggild, et al., (2015). Science and technology roadmap for graphene, related two-dimensional crystals, and hybrid systems. Nanoscale, 7(11), 4598–4810. https://doi.org/10.1039/c4nr01600a

[3] O.C. Compton, S.T. Nguyen, (2010). Graphene oxide, highly reduced graphene oxide, and graphene: Versatile building blocks for carbon-based materials. Small, 6(6), 711–723. https://doi.org/10.1002/smll.200901934

[4] X. Wang, L. Zhi, K. Müllen, (2008). Transparent, conductive graphene electrodes for dye-sensitized solar cells. Nano Lett., 8(1), 323–327. https://doi.org/10.1021/nl072838r

[5] J.B. Wu, H.A. Becerril, Z.N. Bao, Z.F. Liu, Y.S. Cheng, P. Peumans, (2008). Organic solar cells with solution-processed graphene transparent electrodes. Appl. Phys. Lett., 92(26), 263302. https://doi.org/10.1063/1.2924771

[6] Q. Liu, Z.F. Liu, X.Y. Zhang, N. Zhang, L.Y. Yang, S.G. Yin, Y. Chen, (2008). Organic photovoltaic cells based on an acceptor of soluble graphene. Appl. Phys. Lett., 92(22), 223303. https://doi.org/10.1063/1.2938865

[7] W.J. Hong, Y.X. Xu, G.W. Lu, C. Li, G.Q. Shi, (2008). Transparent graphene/PEDOT–PSS composite films as counter electrodes of dye-sensitized solar cells. Electrochem. Commun., 10(10), 1555–1558. https://doi.org/10.1016/j.elecom.2008.08.007

[8] X.L. Li, X.R. Wang, L. Zhang, S.W. Lee, H.J. Dai, (2008). Chemically derived ultrasmooth graphene nanoribbon semiconductors. Science, 319(5867), 1229–1232. https://doi.org/10.1126/science.1150878

[9] L.F. Mao, X.J. Li, Z.O. Wang, J.Y. Wang, (2008). The gate leakage current in graphene field-effect

transistor. IEEE Electron Device Lett., 29(9), 1047–1049. https://doi.org/10.1109/LED.2008.2001475

[10] Y.K. Yoon, G.L. Fiori, S.M. Hong, G. Iannaccone, J. Guo, (2008). Performance Comparison of Graphene Nanoribbon FETs With Schottky Contacts and Doped Reservoirs. IEEE Trans. Electron Devices, 55(9), 2314–2323. https://doi-org.dbvista.idm.oclc.org/10.1109/TED.2008.928021

[11] C. Józsa, T. Maassen, M. Popinciuc, P.J. Zomer, A. Veligura, H.T. Jonkman, B.J. van Wees, (2009). Linear scaling between momentum and spin scattering in graphene. Phys. Rev. B, 80(24), 241403(R). https://doi.org/10.1103/PhysRevB.80.241403

[12] V. Ryzhii, M. Ryzhii, A. Satou, T. Otsuji, (2008). Current-voltage characteristics of a graphene nanoribbon field-effect transistor. J. Appl. Phys., 103(9), 094510. https://doi.org/10.1063/1.2917284

[13] Y. Lin, F. Ding, B.I. Yakobson, (2008). Hydrogen storage by spillover on graphene as a phase nucleation process. Phys. Rev. B, 78(4), 041402. https://doi.org/10.1103/PhysRevB.78.041402

[14] N. Park, S. Hong, G. Kim, S.H. Jhi, (2007). Computational study of hydrogen storage characteristics of covalent-bonded graphenes. J. Am. Chem. Soc., 129(29), 8999–9003. https://doi.org/10.1021/ja0703527

[15] M.D. Stoller, S. Park, Y. Zhu, J. An, R.S. Ruoff, (2008). Graphene-based ultracapacitors. Nano Lett., 8(10), 3498–3502. https://doi.org/10.1021/nl802558y

[16] S.R.C. Vivekchand, C.S. Rout, K.S. Subrahmanyam, A. Govindaraj, C.N.R. Rao, (2008). Graphene-based electrochemical supercapacitors. J. Chem. Sci., 120(1), 9–13.
https://doi.org/10.1007/s12039-008-0002-7

[17] F. Scarpa, S. Adhikari, A. S. Phani, (2009). Effective elastic mechanical properties of single layer graphene sheets. Nanotechnol., 20(6), 065709. https://doi.org/10.1088/0957-4484/20/6/065709

[18] C. Lee, X. Wei, J.W. Kysar, J. Hone, (2008). Measurement of the Elastic Properties and Intrinsic Strength of Monolayer Graphene. Science, 321(5887), 385–388. https://doi.org/10.1126/science.1157996

[19] H.C. Schniepp, J.L. Li, M.J. McAllister, H. Sai, M. Herrera-Alonso, D.H. Adamson, et al., (2006). Functionalized single graphene sheets derived from splitting graphite oxide. J. Phys. Chem. B, 110(17), 8535–8539. https://doi.org/10.1021/jp060936f

[20] M.J. McAllister, J.L. Li, D.H. Adamson, H.C. Schniepp, A.A. Abdala, J. Liu, et al., (2007). Single sheet functionalized graphene by oxidation and thermal expansion of graphite. Chem. Mater., 19(18), 4396–4404. https://doi.org/10.1021/cm0630800

[21] S. Stankovich, R.D. Piner, S.T. Nguyen, R.S. Ruoff, (2006). Synthesis and exfoliation of isocyanate-treated graphene oxide nanoplatelets. Carbon, 44(15), 3342–3347. https://doi.org/10.1016/j.carbon.2006.06.004

[22] T. Zhang, Q. Xue, S. Zhang, M. Dong, (2012). Theoretical approaches to graphene and graphene-based materials. Nano Today, 7(3), 180–200. https://doi.org/10.1016/j.nantod.2012.04.006

[23] R. Faccio, P.A. Denis, H. Pardo, C. Goyenola, A.W. Mombrú, (2009). Mechanical properties of graphene nanoribbons. J. Phys.: Condens. Matter, 21(28), 285304.
https://doi.org/10.1088/0953-8984/21/28/285304

[24] C. Gómez-Navarro, M. Burghard, K. Kern, (2008). Elastic Properties of Chemically Derived Single

Graphene Sheets. Nano Lett., 8(7), 2045–2049. https://doi.org/10.1021/nl801384y

[25] K. Min, N.R. Aluru, (2011). Mechanical properties of graphene under shear deformation. Appl. Phys. Lett., 98(1), 013113. https://doi.org/10.1063/1.3534787

[26] S. Zhao, J. Xue, (2013). Mechanical properties of hybrid graphene and hexagonal boron nitride sheets as revealed by molecular dynamic simulations. J. Phys. D: Appl. Phys., 46(13), 135303. https://doi.org/10.1088/0022-3727/46/13/135303

[27] C.D. Reddy, S. Rajendran, K.M. Liew, (2006). Equilibrium configuration and continuum elastic properties of finite sized graphene. Nanotechnol., 17(3), 864–870.
https://doi.org/10.1088/0957-4484/17/3/042

[28] Y.Y. Zhang, Y.T. Gu, (2013). Mechanical properties of graphene: Effects of layer number, temperature and isotope. Comput. Mater. Sci., 71, 197–200. https://doi.org/10.1016/j.commatsci.2013.01.032

[29] O.C. Compton, S.W. Cranford, K.W. Putz, Z. An, L.C. Brinson, M.J. Buehler, S.T. Nguyen, (2012). Tuning the mechanical properties of graphene oxide paper and its associated polymer nanocomposites by controlling cooperative intersheet hydrogen bonding. ACS Nano, 6(3), 2008–2019. https://doi.org/10.1021/nn202928w

[30] J.T. Paci, T. Belytschko, G.C. Schatz, (2007). Computational studies of the structure, behavior upon heating and mechanical properties of graphite oxide. J. Phys. Chem. C, 111(49), 18099–18111. https://doi.org/10.1021/jp075799g

[31] P. Nayebi, E. Zaminpayma, (2016). A molecular dynamic simulation study of mechanical properties of graphene–polythiophene composite with Reax force field. Phys. Lett. A, 380(4), 628–633. https://doi.org/10.1016/j.physleta.2015.11.026

[32] I.W. Frank, D.M. Tanenbaum, A.M. van der Zande, P.L. McEuen, (2007). Mechanical properties of suspended graphene sheets. J. Vac. Sci. Technol. B, 25(6), 2558–2561. https://doi.org/10.1116/1.2789446

[33] Y. W. Sun, D. G. Papageorgiou, C. J. Humphreys, D. J. Dunstan, P. Puech, J. E. Proctor, C. Bousige, D. Machon, A. San-Miguel, (2021). Mechanical Properties of Graphene. Appl. Phys. Rev. 8, 021310.
https://doi.org/10.1063/5.0040578

[34] S. Stankovich, D.A. Dikin, G.H.B. Dommett, K. M. Kohlhaas, E.J. Zimney, E.A. Stach, et al., (2006). Graphene-based composite materials. Nat., 442(7100), 282–286. https://doi.org/10.1038/nature04969

[35] T. Ramanathan, A.A. Abdala, S. Stankovich, D.A. Dikin, M. Herrera-Alonso, R.D. Piner, et al., (2008). Functionalized graphene sheets for polymer nanocomposites. Nat. Nanotechnol., 3(6), 327–331. https://doi.org/10.1038/nnano.2008.96

[36] J. Longun, O.J. Iroh, (2012). Nano-graphene/polyimide composites with extremely high rubbery plateau modulus. Carbon, 50(5), 1823–1832. https://doi.org/10.1016/j.carbon.2011.12.032

[37] D. Nguyen-Trong, (2020). Z-AXIS deformation method to investigate the influence of system size, structure phase transition on mechanical properties of bulk nickel. Mater. Chem. Phys., 252, 123275. https://doi.org/10.1016/j.matchemphys.2020.123275

[38] D. Nguyen Trong, V. Cao Long, Ş. Ţălu, (2023). The influence of shape and matrix size on the mechanical

properties of the 2D epoxy thin film by Monte Carlo simulation method. AIP Adv., 13(1), 015209. https://doi.org/10.1063/5.0138329

[39] S. Plimpton, (1995). Fast Parallel Algorithms for Short-Range Molecular Dynamics. J. Comput. Phys., 117(1), 1–19. https://doi.org/10.1006/jcph.1995.1039

[40] S. G. Srinivasan, A.C.T. van Duin, P. Ganesh, (2015). Development of a ReaxFF Potential for Carbon Condensed Phases and Its Application to the Thermal Fragmentation of a Large Fullerene. J. Phys. Chem. A, 119(4), 571–580. https://doi.org/10.1021/jp510274e